Journal of Alloys and Compounds 599 (2014) 78–86

Contents lists available at ScienceDirect

Journal of Alloys and Compounds

journal homepage: www.elsevier.com/locate/jalcom

$2LiBH_4$–MgH_2–$0.13TiCl_4$ confined in nanoporous structure of carbon aerogel scaffold for reversible hydrogen storage

Rapee Gosalawit-Utke [a,b,*], Chiara Milanese [c], Payam Javadian [d], Alessandro Girella [c], Daniel Laipple [a], Julián Puszkiel [a], Alice S. Cattaneo [e], Chiara Ferrara [e], Jatuporn Wittayakhun [b], Jørgen Skibsted [d], Torben R. Jensen [d], Amedeo Marini [c], Thomas Klassen [a], Martin Dornheim [a]

[a] Institute of Materials Research, Helmholtz–Zentrum Geesthacht, Geesthacht 21502, Germany
[b] School of Chemistry, Institute of Science, Suranaree University of Technology, Nakhon Ratchasima 30000, Thailand
[c] Pavia Hydrogen Lab, C.S.G.I.-Department of Chemistry-Physical Chemistry Division, University of Pavia, Pavia 27100, Italy
[d] Center for Energy Materials, iNANO and Department of Chemistry, University of Aarhus, Aarhus C8000, Denmark
[e] Department of Chemistry-Physical Chemistry Division, University of Pavia, Pavia 27100, Italy

ARTICLE INFO

Article history:
Received 3 November 2013
Received in revised form 4 February 2014
Accepted 7 February 2014
Available online 15 February 2014

Keywords:
Nanoconfinement
Eutectic $LiBH_4$–$Mg(BH_4)_2$
Magnesium borohydride
$TiCl_4$
Lithium–titanium borohydride

ABSTRACT

The investigations based on kinetic improvement and reaction mechanisms during melt infiltration, dehydrogenation, and rehydrogenation of nanoconfined $2LiBH_4$–MgH_2–$0.13TiCl_4$ in carbon aerogel scaffold (CAS) are proposed. It is found that $TiCl_4$ and $LiBH_4$ are successfully nanoconfined in CAS, while MgH_2 proceeds partially. In the same temperature (25–500 °C) and time (0–5 h at constant temperature) ranges nanoconfined $2LiBH_4$–MgH_2–$0.13TiCl_4$ dehydrogenates completely 99% of theoretical H_2 storage capacity, while that of nanoconfined $2LiBH_4$–MgH_2 is only 94%. Nanoconfined $2LiBH_4$–MgH_2–$0.13TiCl_4$ performs three-step dehydrogenation at 140, 240, and 380 °C. Onset (the first-step) dehydrogenation temperature (140 °C), significantly lower than those of nanoconfined sample of $2LiBH_4$–MgH_2 and $2LiBH_4$–MgH_2–$TiCl_3$ (ΔT = 140 and 110 °C, respectively) is in agreement with the decomposition of eutectic $LiBH_4$–$Mg(BH_4)_2$ and lithium–titanium borohydride. For the second and third steps (240 and 380 °C), decompositions of $LiBH_4$ destabilized by LiCl solvation and MgH_2 are accomplished, respectively. In conclusion, dehydrogenation products are B, Mg, LiH, and TiH. Reversibility of nanoconfined $2LiBH_4$–MgH_2–$0.13TiCl_4$ sample is confirmed by the recovery of $LiBH_4$ after rehydrogenation together with the formation of $[B_{12}H_{12}]^{-}$ derivatives. The superior kinetics during the 2nd, 3rd, and 4th cycles of nanoconfined $2LiBH_4$–MgH_2–$0.13TiCl_4$ to the nanoconfined $2LiBH_4$–MgH_2 can be due to the formations of Ti–MgH_2 alloys ($Mg_{0.25}Ti_{0.75}H_2$ and Mg_6TiH_2) during the 1st rehydrogenation.

1. Introduction

Lithium borohydride ($LiBH_4$), storing 13.8 wt.% H_2 according to the chemical reaction of $LiBH_4 \leftrightarrow LiH + B + 3/2H_2$, is an attractive candidate as a reversible hydrogen storage material. However, high thermodynamic stability and kinetic restrictions obstruct its ability to release and uptake hydrogen at moderate condition [1–3]. To destabilize $LiBH_4$ by the concept of reactive hydride composites (RHCs), MgH_2 is well known as one of the most promising destabilizing agents [4,5]. The RHC composed of $2LiBH_4$–MgH_2 starts to release hydrogen at about 350 °C and complete below 500 °C. Two-step dehydrogenation reaction under H_2 pressure of $\geqslant$3 bar is observed as shown in the following reaction [4,6,7]:

$$2LiBH_4 + MgH_2 \rightarrow 2LiBH_4 + Mg + H_2 \rightarrow 2LiH + MgB_2 + 4H_2. \quad (1)$$

On the basis of reaction (1), not only sluggish kinetics; that is, more than 25 h needed to complete dehydrogenation [5], is observed, but also high temperature (more than 400 °C) is required to obtain reasonable dehydrogenation rate. Several approaches have been investigated to improve de-/rehydrogenation properties of $2LiBH_4$–MgH_2 composite, for example, additive doping [8–18] and particle size reduction [19–22]. Bösenberg et al. [11] reported the addition of several catalysts (titanium isopropoxide (Tiso), SiO_2, and VCl_3) to $2LiBH_4$–MgH_2 composite. Among them, the sample of $2LiBH_4$–MgH_2 with 5 wt.% Tiso performed the best desorption kinetics based on ten times faster dehydrogenation rate than milled $2LiBH_4$–MgH_2 under the same temperature and pressure

* Corresponding author at: School of Chemistry, Institute of Science, Suranaree University of Technology, Nakhon Ratchasima 30000, Thailand
E-mail address: rapee.g@sut.ac.th (R. Gosalawit-Utke).

http://dx.doi.org/10.1016/j.jallcom.2014.02.032
0925-8388/

conditions. Furthermore, other transition metal fluoride [12–15] and chloride [16–18] additives were doped to $2LiBH_4$–MgH_2 composite via mechanical milling, resulting in lower dehydrogenation temperature than neat $2LiBH_4$–MgH_2. For instance, $2LiBH_4$–MgH_2 doped with NbF_5 exhibited the best performance by starting dehydrogenation at about 300 °C and allowing complete dehydrogenation below 450 °C [12,13]. For particle size reduction, high-energy mechanical milling has been thoroughly conducted to prepare $2LiBH_4$–MgH_2 nanoparticle. Nevertheless, particle agglomeration and grain growth were clearly detected upon hydrogen release and uptake cycles [16]. Nanoconfinement of metal hydrides (MgH_2 [23] and Mg–MgH_2 [24]), complex hydrides ($LiBH_4$ [25,26], $Mg(BH_4)_2$ [27], and $NaAlH_4$ [28]), and RHCs ($LiBH_4$–$Ca(BH_4)_2$ [29] and $LiBH_4$–MgH_2 [19–21]) in various types of carbon hosts has been recently of interest. After nanoconfinement, the porous structure of carbon host provides not only constraining particle growth of the hydride composites upon cycling, but also shortening diffusion lengths for hydrogen exchange reaction [30,31].

The $2LiBH_4$–MgH_2 composite was successfully nanoconfined in an inert carbon aerogel scaffolds via either solution impregnation [19] or direct melt infiltration [20,21], leading to the improvement of desorption kinetics. Nanoconfined $2LiBH_4$–MgH_2 showed ten-time faster reaction rate and lower activation energy ($\Delta E_A \sim 89 \pm 2$ kJ/mol for MgH_2 decomposition [32]) as compared with milled sample. Afterward, kinetic properties of nanoconfined $2LiBH_4$–MgH_2 have been further developed by $TiCl_3$ doping via solution impregnation [33]. The nanoconfined sample with $TiCl_3$ completed dehydrogenation within 2 h, while those of the nanoconfined sample without catalyst and bulk material required 4 and 25 h, respectively. Moreover, since only 1.6 wt.% $TiCl_3$ (with respect to the amount carbon aerogel) was doped in the carbon host, up to 99% of theoretical hydrogen storage capacity was reversible after four release and uptake cycles. However, it was found that onset dehydrogenation temperatures of nanoconfined samples with and without $TiCl_3$ were comparable at about 250 °C. This informs that the insignificant amount of catalyst (only 1.6 wt.% $TiCl_3$ with respect to carbon aerogel content) does not influence the reaction pathway based on the new reactive phase formation during dehydrogenation and/or nanoconfinement of nanoconfined $2LiBH_4$–MgH_2. It was previously reported that by milling $LiBH_4$:$TiCl_4$ (8:2 M ratio), ion-exchange interaction between $LiBH_4$ and $TiCl_4$ to produce $Ti(BH_4)_3$ and LiCl was obtained, where $Ti(BH_4)_3$ decomposed and released hydrogen and toxic diborane (B_2H_6) gas at 25 °C [34]. In the case of $TiCl_3$, however, the formation of $Ti(BH_4)_3$ was not successfully achieved from both milled samples of $LiBH_4$–$0.2MgCl_2$–$0.1TiCl_3$ [35] and $LiBH_4$–$0.5TiCl_3$ [36].

For the present work, on one hand further investigation with respect to kinetic effects of the other well-known Ti-based catalyst (titanium (IV) chloride, $TiCl_4$) on nanoconfined $2LiBH_4$–MgH_2 in carbon aerogel scaffold is considered. On the other hand, the interactions between $LiBH_4$ both with $TiCl_4$ and MgH_2, resulting in the formation of new reactive phases and reduction of dehydrogenation temperature is of interest. Carbon aerogel scaffold prepared from resorcinol-formaldehyde aerogel is embedded with $TiCl_4$ via solution impregnation and it is continuously melt infiltrated with milled $2LiBH_4$–MgH_2 to obtain nanoconfined $2LiBH_4$–MgH_2–$0.13TiCl_4$ sample. Successful confinement of $2LiBH_4$–MgH_2–$0.13TiCl_4$ composite are investigated by N_2 adsorption–desorption, scanning electron microscopy (SEM), and energy-dispersive X-ray spectroscopy (EDS) experiments. Reaction mechanisms during infiltration, dehydrogenation and rehydrogenation are determined by in situ synchrotron radiation powder X-ray diffraction (SR-PXD), solid-state boron-11 magic-angle spinning nuclear magnetic resonance (solid-state ^{11}B MAS NMR), and Fourier transform infrared spectroscopy (FTIR). Gases released during dehydrogenation are determined by gas analysis technique. Kinetic properties are investigated by coupled manometric–calorimetric and titration measurements.

2. Experimental details

2.1. Sample preparation

Resorcinol-formaldehyde (RF) aerogels were synthesized according previous procedures [37]. The mixture of 41.4290 g resorcinol (99%, Aldrich), 56.66 mL deionized water, 56.92 mL formaldehyde solution (37 wt.% formaldehyde solution in water stabilized by 10–15 wt.% methanol, Sigma–Aldrich), and 0.0340 g anhydrous Na_2CO_3 (99.999%, Aldrich) was continuously stirred until homogeneity. The polymer solution sealed in polypropylene bottles was aged at room temperature for 24 h, 50 °C for 24 h, 90 °C for 72 h, and cooled to room temperature. The aerogels achieved was soaked in an acetone bath three times within 3–4 days and dried at room temperature for several days in the fume hood. The dried aerogels were cut into small pieces (ca. 0.4 cm^3) and carbonized in a tubular oven at constant temperature of 800 °C (2.6 C/min) for 6 h under N_2 flow. The furnace was turned off and the samples were cooled down to room temperature. The gel obtained was further treated at 500 °C under vacuum for 16 h to obtain a carbon aerogel scaffold, denoted as CAS.

The mixture of 5.3442 g $LiBH_4$ (90 + % hydrogen-storage grade, Aldrich) and 3.1580 g MgH_2 (hydrogen-storage grade, Aldrich) was milled in a molar ratio of 2:1 ($LiBH_4$:MgH_2) in a stainless steel vial (Evico Magnetic, Germany) by using a Fritsch Pulverisette 6 classic line planetary mill under an argon atmosphere in a glove box. Milling was carried out for 5 h (at 400 rpm) with a ball-to-powder weight ratio (BPR) of 10:1 to obtain milled $2LiBH_4$–MgH_2.

Titanium (IV) chloride ($TiCl_4$) was embedded in CAS solution impregnation. The powder of CAS (0.8384 g) was immersed in 15.00 mL of $TiCl_4$ solution (1 M $TiCl_4$ in methylene chloride, Sigma–Aldrich). The solution was left at room temperature for several days in the glove box until the solvent was completely evaporated. The CAS impregnated with $TiCl_4$ of 1.0223 g was obtained and denoted as $TiCl_4$–CAS. The powder of milled $2LiBH_4$–MgH_2 was ground with $TiCl_4$–CAS in the mortar with a weight ratio of 1:2 (milled $2LiBH_4$–MgH_2: $TiCl_4$–CAS) to obtain the mixture of $2LiBH_4$–MgH_2–$TiCl_4$–CAS. Nanoconfinement was carried out by using a Sievert-type apparatus (a PCTPro-2000, Hy-Energy LLC). The powder samples of $2LiBH_4$–MgH_2–$TiCl_4$–CAS was heated to 310 °C (5 °C/min) under 60 bar H_2, dwelled at 310 °C for 30 min, and cooled to room temperature to achieve nanoconfined sample with the molar ratio of 2:1:0.13 ($LiBH_4$:MgH_2:$TiCl_4$), denoted as nanoconfined $2LiBH_4$–MgH_2–$0.13TiCl_4$. For comparison, nanoconfined $2LiBH_4$–MgH_2 without catalyst was also prepared by the same weight ratio and procedures.

2.2. Characterizations

The texture parameters of CAS, $TiCl_4$–CAS, and nanoconfined $2LiBH_4$–MgH_2–$0.13TiCl_4$ were characterized by N_2 adsorption–desorption measurements using a Nova 2000e surface area and pore size analyzer from Quantachrome. Prior to the measurements, a known amount of sample was degassed at 120 °C under vacuum for several hours. All samples were studied with a full adsorption and desorption isotherm in the pressure range of 0–1 p/p_0 at liquid nitrogen temperatures with nitrogen gas as an adsorbent. The measurement was programed to continuously change the pressure ratio to 1 for adsorption, and to 0 for desorption. Data were analyzed by t-plot method [38,39], the Brunner Emmet Teller (BET) method [40], and the Barret Joyner Halenda (BJH) method [41], and the highest point of the isotherm measurements (where $p/p_0 \sim 1$) was used to calculate the total volume of the sample.

The powder sample of nanoconfined $2LiBH_4$–MgH_2–$0.13TiCl_4$ was deposited on the sample holder by using silver glue (in n-butylacetate) and coated by palladium–gold (Pd–Au) sputtering with a current of 30 mA for 30 s under vacuum. The sample coated with Pd–Au was loaded in a scanning electron microscope (SEM, an Auriga instrument from Zeiss, Germany). via focus ion beam (FIB) technique, the surface of the powder sample was irradiated by a gallium (Ga) ion beam with an energy of 30 kV to create an internal area of the sample bulk ($20 \times 20 \times 6\ \mu m^3$). An energy-dispersive X-ray spectroscopy (EDS) (an EDAX Inc., USA) and an EDS Genesis program, installed in the SEM instrument, were used to analyze the elemental components on the surface and inside the sample bulk.

Coupled manometric–calorimetric measurements of the nanoconfined samples of $2LiBH_4$–MgH_2, and $2LiBH_4$–MgH_2–$0.13TiCl_4$ were carried out by using a high–pressure calorimeter (a Sensys DSC, Setaram) connected to a Sievert-type apparatus (a PCTPro-2000, Setaram & Hy-Energy) by a 1/8 in stainless steel tube. The high-pressure cell of the calorimeter was loaded with ~13–25 mg of the powder sample in the glove box. Dehydrogenation was performed by heating the sample from room temperature up to 550 °C with heating rate of 5 °C/min under 3 bar H_2 overpressure. The calorimetric profiles were evaluated by a Calisto software to obtain the peak temperatures.

The investigation of gases evolved upon dehydrogenation of nano $2LiBH_4$–MgH_2–$0.13TiCl_4$ sample was carried out by connecting the manometric PCTPro-2000 apparatus with a residual gas analyzer RGA200 (Setaram, France) by using a

1/8" stainless steel tube. The powder sample of ~200 mg was loaded in the sample holder and assembled to the PCTPro-2000 apparatus. The sample was heated from room temperature to 500 °C at 5 °C/min under 3–4 bar H_2. The signal of the gases released from the sample was recorded in continuum.

The kinetic properties based on dehydrogenation, rehydrogenation and cycling efficiency of nanoconfined $2LiBH_4$–MgH_2–$0.13TiCl_4$ were studied by a carefully calibrated Sievert-type apparatus (a PCTPro-2000, Hy-Energy LLC). The powder sample (~200 mg) was loaded into a high pressure-temperature vessel and transferred to the Sievert-type apparatus. Dehydrogenation was done at 425 °C (5 °C/min) under 3.4 bar H_2 overpressure. For rehydrogenation, the dehydrogenated powder was heated to 425 °C (5 °C/min) under hydrogen pressure of 130 bar and kept at 425 °C for 12 h. For comparison, nanoconfined $2LiBH_4$–MgH_2 was also dehydrogenated and rehydrogenated by similar procedures.

In situ synchrotron radiation powder X-ray diffraction (SR-PXD) experiments were performed at the MAX II Synchrotron, beamline I711 in the MAX-Lab Research Laboratory, Lund, Sweden [42]. The powder diffraction patterns were recorded by a MAR165 CCD detector with an image plate (X7B) and a Simens CCD area detector (X6B). The selected X-ray wavelength was 0.999991 Å. A sample cell was specially developed to study gas/solid reactions and allows high pressure and temperature to be applied [43,44]. The powder sample was packed tightly in the sapphire capillary in the glove box. The temperature was controlled by a thermocouple placed in the sapphire capillary next to the sample. Infiltration was carried out by heating the mixtures of milled $2LiBH_4$–MgH_2 and $TiCl_4$–CAS to 335 °C (10 °C/min) under 60 bar H_2, dwelling at 335 °C for 30 min, and cooling to room temperature. For dehydrogenation, the nanoconfined sample was continuously heated to 450 °C (10 °C/min) under 1–5 bar H_2 overpressure, kept at 450 °C for 1 h, and cooled to room temperature. Rehydrogenation was accomplished by heating the dehydrogenated sample to 450 °C (10 °C/min) under 130 bar H_2, keeping at 450 °C for 1 h, and cooling to room temperature. The FIT2D program was used to remove diffraction spots of the sapphire sample holder and to transform raw data to diffraction patterns.

Solid–state MAS NMR spectra were recorded on a Varian Direct–Drive VNMRS-600 and a Bruker Avance III 400 MHz spectrometers. ^{11}B MAS NMR experiments performed by a Varian Direct–Drive VNMRS-600 used a home-built CP/MAS NMR probe for 4 mm outer diameter rotors. The experiments employed a spinning speed of 12 kHz, a 0.5 μs excitation pulse for a ^{11}B rf field strength of $\gamma B1/2\pi \approx 60$ kHz, and a 10-s relaxation delay. In the case of the experiments done by Bruker Avance III 400 MHz, it was carried out at 128.4 MHz at room temperature in a 4 mm MAS NMR probe, where the spinning frequency was 10 kHz. A single pulse of 1.20 μs (30° solid flip angle) and a recycle delay of 6 s were selected. The probe background due to the boron nitride stator was mathematically removed. Chemical shifts were reported relative to BF_3–Et_2O solution. The samples were diluted with anhydrous KBr powder to achieve a complete filling of the rotor. The deconvolution of ^{11}B NMR spectra was done by using a curve fitting program named MagicPlot.

The powder samples of nanoconfined $2LiBH_4$–MgH_2–$0.13TiCl_4$ after dehydrogenation and rehydrogenation as well as pristine $LiBH_4$ were characterized by Fourier transform infrared spectroscopy (FTIR) using a Bruker Equinox 55. The powder sample was ground with anhydrous KBr in the mortar with a weight ratio of approximately 10:1 (KBr:powder sample). The mixture was pressed under specific pressure to obtain KBr pellet. The KBr pellet containing the sample was assembled in the sample holder located in the direction of infrared radiation. The FTIR spectra were collected in the wave length of 3000–500 cm^{-1} with 64 scans for both samples and background.

3. Results and discussion

3.1. Nanoconfinement of $TiCl_4$ and hydride composite

To confirm successful nanoconfinement of $TiCl_4$ and hydride composite in CAS, N_2 adsorption–desorption, scanning electron microscopy (SEM), and energy-dispersive X-ray spectroscopy (EDS) were carried out. From Table 1, CAS used in this study shows a surface area, a pore size, and a total pore volume of 659 m^2/g, 26 nm, and 1.30 mL/g, respectively. After $TiCl_4$ impregnation, the surface area of $TiCl_4$–CAS decreases significantly to 78.0 m^2/g, in agreement with the reduction of their microporous (pore size < 2 nm) and mesoporous (2 nm < pore size < 50 nm) volumes. This implies successful impregnation of $TiCl_4$ in both micropores and mesopores of CAS. After melt infiltration of milled $2LiBH_4$–MgH_2, the surface area and total pore (mesopore and total pore) volume of nanoconfined $2LiBH_4$–MgH_2–$0.13TiCl_4$ decrease to 45 m^2/g and 0.31 mL/g, respectively, suggesting successful nanoconfinement of hydride composite. In addition, SEM-EDS and focus ion beam (FIB) techniques were used to investigate the elemental compositions on the surface and inside CAS. Fig. 1(A) reveals rough surface morphology of nanoconfined $2LiBH_4$–MgH_2–$0.13TiCl_4$ sample. The elemental analysis on the surface of nanoconfined $2LiBH_4$–MgH_2–$0.13TiCl_4$ gives the signals of carbon (C) and oxygen (O) from CAS and oxidation in air, respectively, as well as those of magnesium (Mg). silicon (Si), and gold (Au) from MgH_2, contamination, and sputtering element, respectively (Fig. 1(B)). Fig. 1(C) shows the internal area of sample specimen, where EDS technique is carried out to study the elemental compositions inside the sample bulk. From Fig. 1(D), the signals of C, O, and Si are still detected as found on the surface together with those of gallium (Ga), Mg, chlorine (Cl), and Ti from FIB technique, MgH_2 and $TiCl_4$, respectively. From EDS results, it should be noted that MgH_2 is found both on the surface and in the bulk of nanoconfined $2LiBH_4$–MgH_2–$0.13TiCl_4$ sample, while $TiCl_4$ is almost completely nanoconfined. With respect to the limitation of EDS technique, which is not sensitive to the light elements, the signals of lithium (Li) and boron (B) of $LiBH_4$ are not observed. Nevertheless, coupled manometric–calorimetric and in situ synchrotron radiation powder X-ray diffraction (SR-PXD) techniques, further discussed in Sections 3.2 and 3.4, can confirm the nanoconfinement of $LiBH_4$ in $TiCl_4$–CAS.

The amount of $TiCl_4$ with respect to CAS content (mol%) and theoretical hydrogen storage capacity (wt.% H_2) of all nanoconfined samples were calculated based on proportion of each component and dehydrogenation reaction of hydride composite as followed:

$$2LiBH_{4(l)} + MgH_{2(s)} \leftrightarrow 2LiH_{(s)} + MgB_{2(s)} + 4H_{2(g)}. \quad (2)$$

Nanoconfined $2LiBH_4$–MgH_2 contains 66.7, 21.0, and 12.3 wt.% of CAS, $LiBH_4$, and MgH_2, respectively (Table 2). In the case of nanoconfined $2LiBH_4$–MgH_2–$0.13TiCl_4$, 54.7, 12.0, 21.0, and 12.3 wt.% are found for CAS, $TiCl_4$, $LiBH_4$, and MgH_2, respectively. Regarding the dehydrogenation mechanism of $2LiBH_4$–MgH_2 (Reaction (2)) and molar ratio of $LiBH_4$:MgH_2 (2:1), theoretical hydrogen storage capacity of 3.81 wt.% is calculated for both nanoconfined samples (Table 2).

3.2. Dehydrogenation profiles

Preliminary studies on dehydrogenation behavior of nanoconfined $2LiBH_4$–MgH_2 and $2LiBH_4$–MgH_2–$0.13TiCl_4$ were performed by coupled manometric–calorimetric measurements. From Fig. 2(A), nanoconfined $2LiBH_4$–MgH_2 shows structural transformation of $LiBH_4$ (*o*-$LiBH_4$ to *h*-$LiBH_4$) as a single endothermic peak at 107 °C. By heating the sample to 275 °C, an endothermic peak corresponding to melting of *h*-$LiBH_4$ [3,6] is observed without dehydrogenation, confirmed by no weight loss from manometric respond (Fig. 2(A)). For dehydrogenation, nanoconfined $2LiBH_4$–MgH_2 desorbs totally 2.9 wt.% H_2 in the temperature range of 280–500 °C (manometric plot in Fig. 2(A)). In the case of nanoconfined $2LiBH_4$–MgH_2–$0.13TiCl_4$, Fig. 2(B) reveals structural transformation of $LiBH_4$ as multiple endothermic peaks in the temperature range of 80–100 °C. The peaks at 81 and 91 °C are likely from structural transfor-

Table 1
Texture parameters of CAS, $TiCl_4$–CAS, and nanoconfined $2LiBH_4$–MgH_2–$0.13TiCl_4$.

Samples	S_{BET} (m^2/g)	D_{max} (nm)	V_{micro} (mL/g)	V_{meso} (mL/g)	V_{total} (mL/g)
CAS	659	26	0.19	1.10	1.30
$TiCl_4$–CAS	78.0	26	0	0.71	0.67
Nanoconfined $2LiBH_4$–MgH_2–$0.13TiCl_4$	45.0	26	0	0.32	0.31

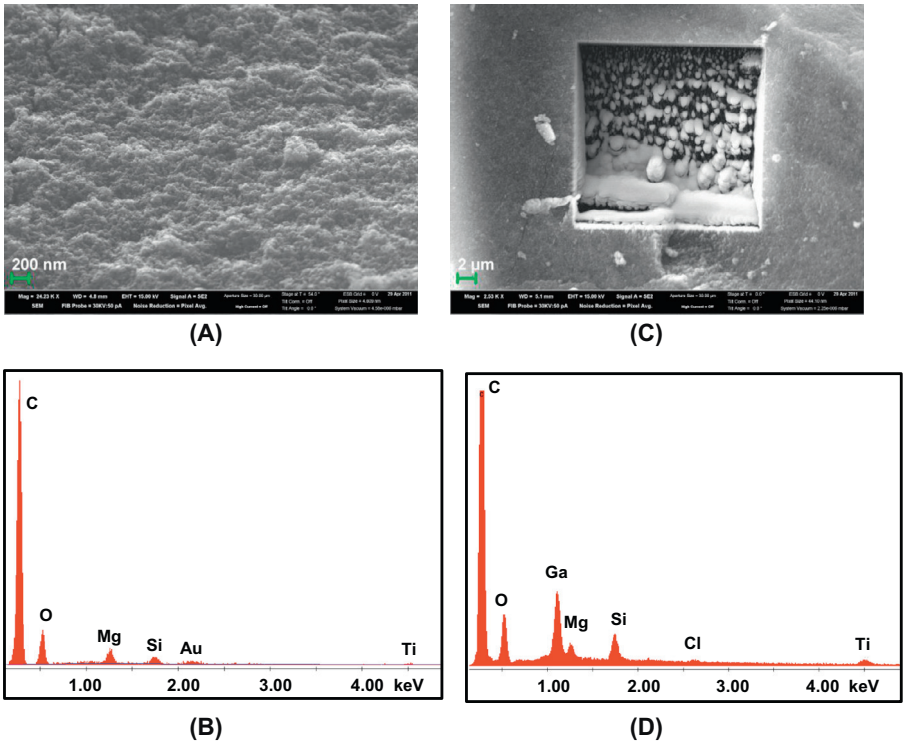

Fig. 1. SEM images and elemental analysis (EDS results) of nanoconfined $2LiBH_4$–MgH_2–$0.13TiCl_4$ on the surface (A) and (B), respectively, and inside the sample bulk (C) and (D), respectively.

Table 2
Proportion of all components, $LiBH_4$:MgH_2:$TiCl_4$ molar ratio, and theoretical hydrogen storage capacity of nanoconfined samples.

Nanoconfined samples	Proportion of components (wt.%)				Molar ratio of $LiBH_4$:MgH_2:$TiCl_4$	Theoretical H_2 storage capacity (wt.% H_2)
	CAS	$TiCl_4$	$LiBH_4$	MgH_2		
$2LiBH_4$–MgH_2	66.7	–	21.0	12.3	2:1:–	3.81
$2LiBH_4$–MgH_2–$0.13TiCl_4$	54.7	12.0	21.0	12.3	2:1:0.13	3.81

mation of $LiBH_4$, which interacts with $TiCl_4$ impregnated in CAS and forms eutectic phase with $Mg(BH_4)_2$, further characterized by solid-state ^{11}B MAS NMR and discussed in Section 3.4, while that at 100 °C, approaching to $LiBH_4$ structural transformation of nanoconfined $2LiBH_4$–MgH_2 (107 °C) can attribute to $LiBH_4$ nanoconfined in CAS (neither interaction with $TiCl_4$ nor eutectic $LiBH_4$–$Mg(BH_4)_2$ formation). With respect to $LiBH_4$ structural transformation of milled $2LiBH_4$–MgH_2 at 117 °C [20], lower temperatures of the same phenomena found in nanoconfined $2LiBH_4$–MgH_2 (107 °C) and $2LiBH_4$–MgH_2–$0.13TiCl_4$ (81, 91, and 100 °C) confirm successful nanoconfinement of $LiBH_4$ in CAS. An endothermic peak at 255 °C belongs not only to *h*-$LiBH_4$ melting, but also to partial dehydrogenation, that is, approximately 0.4 wt.% H_2 release from nanoconfined $2LiBH_4$–MgH_2–$0.13TiCl_4$ (Fig. 2(B)). Interestingly, dehydrogenation of nanoconfined $2LiBH_4$–MgH_2–$0.13TiCl_4$ starts slightly after $LiBH_4$ phase transformation (~140 °C) (manometric curve in Fig. 2(B)), significantly lower than those of nanoconfined $2LiBH_4$–MgH_2 (ΔT = 140 °C) and $2LiBH_4$–MgH_2–$TiCl_3$ (ΔT = 110 °C) [33]. This could be due to the interaction between $LiBH_4$ and $TiCl_4$ nanoconfined in CAS as well as the eutectic $LiBH_4$–$Mg(BH_4)_2$ formation, further clarified by ^{11}B MAS NMR results (Section 3.4). In the case of hydrogen storage capacity, nanoconfined $2LiBH_4$–MgH_2–$0.13TiCl_4$ gives totally 3.4 wt.% in the temperature range of 140–500 °C (Fig. 2(B)). Therefore, in the same temperature range from room temperature to ~500 °C, nanoconfined $2LiBH_4$–MgH_2–$0.13TiCl_4$ desorbs 89% of theoretical hydrogen storage capacity, while that of nanoconfined $2LiBH_4$–MgH_2 is only 76%. This faster dehydrogenation rate suggests kinetic improvement after $TiCl_4$ impregnation and nanoconfinement. It should be also mentioned that both nanoconfined samples (with and without $TiCl_4$) perform a single-step dehydrogenation.

Besides, gas composition released during dehydrogenation of nanoconfined $2LiBH_4$–MgH_2–$0.13TiCl_4$ is monitored by gas analysis technique. From Fig. 3(A), majority of gas desorbed in the temperature range of 30–500 °C is H_2 together with small amount of water (from humidity) and methane (CH_4), hydrochloric (HCl), and unknown (from dichloromethane solvent of $TiCl_4$ solution). In the case of toxic diborane gas (B_2H_6), it is not detected upon dehydrogenation of nanoconfined $2LiBH_4$–MgH_2–$0.13TiCl_4$. To clearly analyze content and onset temperature of gas released, peak area of each gas signal (From Fig. 3(A)) is plotted versus temperature. Fig. 3(B) reveals higher amount of H_2 up to 15 times more than other gases. Interestingly, hydrogen desorption starts approximately at 140 °C, approaching to coupled manometric–calorimetric results of this sample shown in Fig. 2(B). This can be due to the dehydrogenations of (i) $LiBH_4$ interacted with $TiCl_4$ nanoconfined in CAS and (ii) eutectic $LiBH_4$–$Mg(BH_4)_2$ formed during nanoconfinement, further confirmed by ^{11}B MAS NMR results (Fig. 7) and discussed in Section 3.4. Moreover, it is clearly seen that dehydrogenation is carried out as three-step reaction at about 140, 240, and 380 °C (Fig. 3(B)), where the reaction mechanisms is further discussed in Section 3.4.

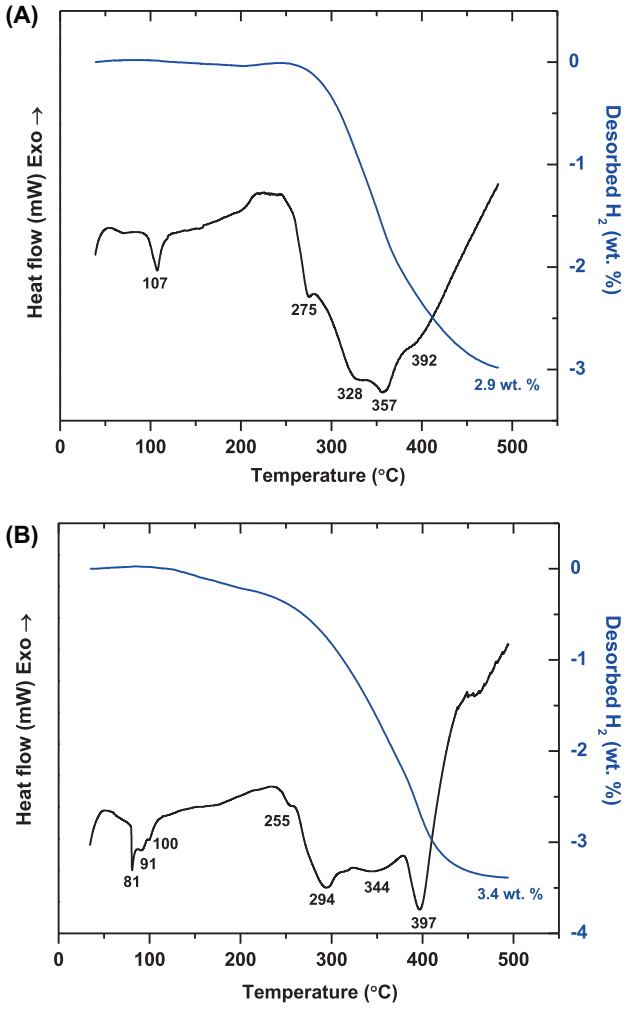

Fig. 2. Coupled nanometric–calorimetric results of nanoconfined samples of $2LiBH_4$–MgH_2 (A) and $2LiBH_4$–MgH_2–$0.13TiCl_4$ (B).

3.3. Kinetics, reversibility, and hydrogen reproducibility

To study kinetic properties, reversibility, and hydrogen reproducibility, titration measurements by Sievert-type apparatus were carried out. Four hydrogen release and uptake cycles of both nanoconfined samples (with and without $TiCl_4$) were performed at 425 °C ($p(H_2)$ = 3.4 bar overpressure) and at 425 °C ($p(H_2)$ = 130 bar for 12 h), respectively. From Fig. 4, nanoconfined $2LiBH_4$–MgH_2 releases 3.6 wt.% H_2 (94% of theoretical H_2 storage capacity) during the 1st dehydrogenation, while that of nanoconfined $2LiBH_4$–MgH_2–$0.13TiCl_4$ is 3.76 wt.% H_2 (99% of theoretical H_2 storage capacity). It should be taken into account that at the same hydrogen content of ~3.6 wt.%, nanoconfined $2LiBH_4$–MgH_2–$0.13TiCl_4$ releases hydrogen approximately twice as fast as the nanoconfined $2LiBH_4$–MgH_2 (the 1st dehydrogenation in Fig. 4). For the 2nd dehydrogenation, to desorb 3 wt.% H_2 nanoconfined $2LiBH_4$–MgH_2 requires up to 7 h, while that of nanoconfined $2LiBH_4$–MgH_2–$0.13TiCl_4$ accomplishes within 3 h. This can be explained by the formations of new hydride phases during rehydrogenation of nanoconfined $2LiBH_4$–MgH_2–$0.13TiCl_4$ sample, discussed in Section 3.4: reaction mechanisms. In the case of the 3rd and 4th cycles (up to 5 h), faster rates are still achieved from nanoconfined $2LiBH_4$–MgH_2–$0.13TiCl_4$ (inset of Fig. 4). After 5 h, both nanoconfined samples (with and without $TiCl_4$) exhibit comparable kinetics. A similar phenomenon found from both nanoconfined samples is comparable dehydrogenation kinetics during the 3rd and 4th cycles, in agreement with the previous studies [20,21,33]. Besides, single-step dehydrogenation is observed in all cycles as similar to the decomposition shown in DSC thermograms (Fig. 2).

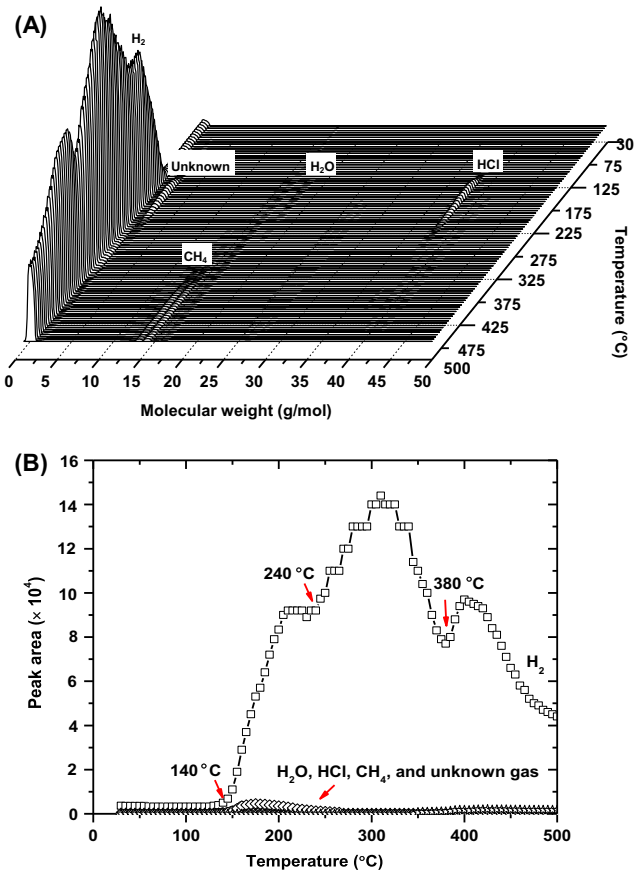

Fig. 3. Gas analysis during dehydrogenation (30–500 °C) of nanoconfined $2LiBH_4$–MgH_2–$0.13TiCl_4$ (A) and peak area of each gas released versus temperature (B).

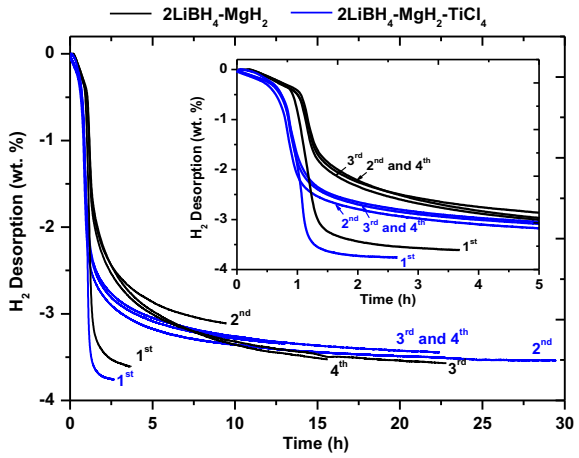

Fig. 4. Dehydrogenation profiles and cycling efficiency of nanoconfined samples of $2LiBH_4$–MgH_2 and $2LiBH_4$–MgH_2–$0.13TiCl_4$.

3.4. Reaction mechanisms

In this section, the reaction mechanisms of nanoconfined $2LiBH_4$–MgH_2–$0.13TiCl_4$ during melt infiltration, dehydrogenation,

and rehydrogenation were studied by in situ synchrotron radiation powder X-ray diffraction (SR–PXD), solid-state boron-11 magic-angle spinning nuclear magnetic resonance (^{11}B MAS NMR), and Fourier transform infrared spectroscopy (FTIR). From Fig. 5, diffraction patterns of *o*-$LiBH_4$, MgH_2, and LiCl as well as a broad region corresponding to a graphite-like structure of CAS in the 2θ range of 10–15° [45] are observed at room temperature. The formation of LiCl (before melt infiltration) refers to the reaction between $LiBH_4$ and $TiCl_4$ during mortar grind of milled $2LiBH_4$–MgH_2 and $TiCl_4$–CAS. Mosegaard et al. [46] noticed that $LiBH_4$ reacts partly with $TiCl_3$ to form LiCl already at room temperature before in situ SR-PXD measurements. By increasing the temperature up to 86 and 244 °C, structural transformation from *o*- to *h*-$LiBH_4$ and melting of *h*-$LiBH_4$ are observed [3], respectively (Fig. 5). At about 275 °C, MgO diffractions arise, while those of MgH_2 decreases. The formation of MgO could be due to the small amount of oxygen in the capillary during the in situ SR-PXD experiments. During isothermal condition (335 °C), the intensity of LiCl enhances, suggesting the further reaction between $LiBH_4$ and $TiCl_4$ during melt infiltration. After cooling, the diffraction patterns of $LiBH_4$ disappear (Fig. 5). The enhancement of LiCl intensity and the disappearance of $LiBH_4$ patterns after melting infiltration hint at nanoconfinement of $LiBH_4$ in $TiCl_4$–CAS. Since $TiCl_4$ is nanoconfined in CAS, the increase of LiCl, referring to the interaction between $LiBH_4$ and $TiCl_4$, suggests the infiltration of $LiBH_4$ in nanopores.

In the case of dehydrogenation under 3 bar H_2, the intensity of LiCl diffraction peaks decreases at about 250 °C (Fig. 6), approaching to melting of *h*-$LiBH_4$ and partial dehydrogenation as shown as an endothermic peak at 255 °C in DSC and TG thermograms (Fig. 2(B)) and hydrogen release at 240 °C (gas analysis in Fig. 3(B)). It was reported and explained in the literature that solid LiCl could be dissolved in the structure of *h*-$LiBH_4$, resulting in the enhancement of structure flexibility and reactivity of $LiBH_4$ [46], probably encourage dehydrogenation of $LiBH_4$. For MgH_2, the onset dehydrogenation temperature is at 360 °C, in accordance with endothermic peak at 344 °C (DSC results in Fig. 2(B)) and last hydrogen desorption step at 380 °C (gas analysis in Fig. 3(B)). In the temperature range of 360–400 °C, MgH_2 desorbs completely, confirmed by the refraction of Mg. Besides, MgO is found at all

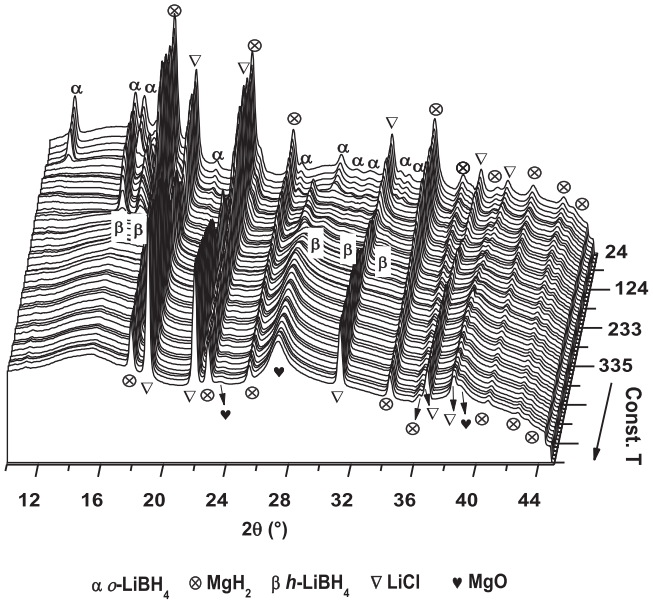

Fig. 5. SR-PXD patterns of nanoconfined $2LiBH_4$–MgH_2–0.13$TiCl_4$ during melt infiltration (T = 335 °C, dT/dt = 10 °C/min, and $p(H_2)$ = 60 bar).

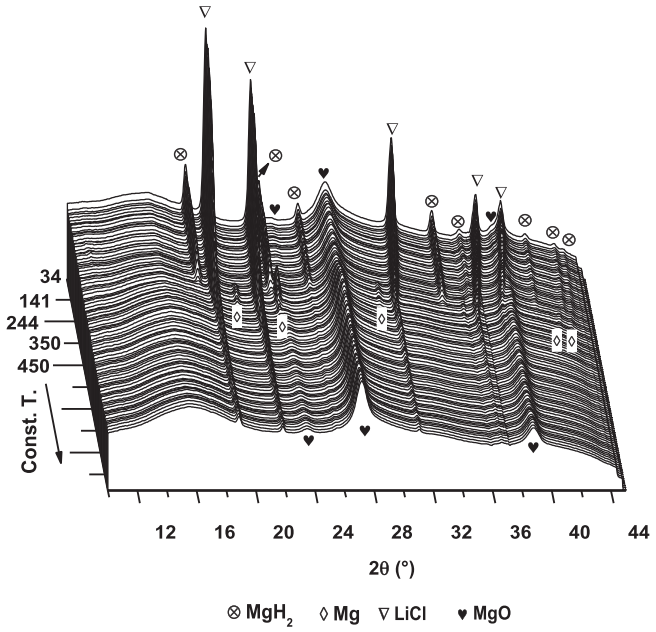

Fig. 6. SR-PXD patterns of nanoconfined $2LiBH_4$–MgH_2–0.13$TiCl_4$ during dehydrogenation (T = 450 °C, dT/dt = 10 °C/min, and $p(H_2)$ = 1–5 bar).

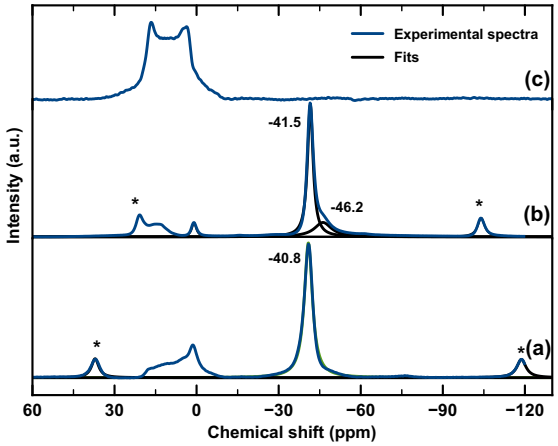

Fig. 7. Solid–state ^{11}B MAS NMR of nanoconfined $2LiBH_4$–MgH_2–0.13$TiCl_4$ after nanoconfinement ((a) and (b)) and after dehydrogenation (c). The spectra (a) and (c) were recorded at 400 MHz, while that of (b) was at 600 MHz. The spinning sidebands are marked by asterisks.

temperature during dehydrogenation. It should be noted that the disappearance of LiH, regularly dehydrogenated from $2LiBH_4$–MgH_2 sample, hints at nanoconfinement in $TiCl_4$–CAS as similar as reported in the previous work [21,32].

From in situ SR-PXD results during melt infiltration and dehydrogenation (Figs. 5 and 6), all phases found are approximately similar to those of nanoconfined $2LiBH_4$–MgH_2–$TiCl_3$ previously reported [33]. This could be due to either no difference in reaction pathway between these two systems or amorphous phases formed due to nanoconfinement. However, the significant reduction of onset dehydrogenation temperature of nanoconfined $2LiBH_4$–MgH_2–0.13$TiCl_4$ (140 °C) as compared with nanoconfined $2LiBH_4$–MgH_2–$TiCl_3$ (250 °C) [33] could refer to different reaction mechanisms and/or new phase formations. Therefore, to determine phases, which promote the reduction of dehydrogenation temperature, ^{11}B MAS NMR technique was performed on the sample after melt infiltration.

In order to avoid the inhomogeneity of the sample bulk, many samplings from nanoconfined $2LiBH_4$–MgH_2–$0.13TiCl_4$ for ^{11}B MAS NMR experiments were carried out. It was found that two different ^{11}B MAS NMR spectra were achieved from nanoconfined $2LiBH_4$–MgH_2–$0.13TiCl_4$ as shown in Figs. 7(a) and (b). Fig. 7 (a) reveals a ^{11}B MAS NMR peak at −40.8 ppm, corresponding to $[BH_4]^-$ units. A similar shift was reported by Zhao-Karger et al. [47] for an eutectic $LiBH_4$–$Mg(BH_4)_2$ phase, centered between the chemical shift of $LiBH_4$(-41.5 ppm) and $Mg(BH_4)_2$ (-40.1 ppm). This suggests a possible reaction between $LiBH_4$ and MgH_2 during melt infiltration to form $Mg(BH_4)_2$. Therefore, the signal can be assigned to $[BH_4]^-$ units of both $LiBH_4$ and $Mg(BH_4)_2$ as well as eutectic $LiBH_4$–$Mg(BH_4)_2$. The other weaker signals in the range of 0–20 ppm are in agreement with B–O bonds [48], e.g., trigonal BO_3 (16–20.9 ppm) and tetrahedral BO_4 (1.0 ppm) units [49], suggesting slight dehydrogenation of BH_4^- and oxidation in ambient condition during nanoconfinement. For the other possible phase formed in nanoconfined $2LiBH_4$–MgH_2–$0.13TiCl_4$, Fig. 7(b) shows the main peak at −41.3 ppm together with a small shoulder at −46.2 ppm, hinting at $LiBH_4$ [47] and a new borohydride phase of lithium-transition metal (Ti) borohydride, respectively. The signals in the 0–20 ppm range come from B–O bonds as in Fig. 7(a), where the slight shift is due to the quadrupolar interactions scaling with the field. Ravnsbæk et al. [50] studied detailed structural, physical, and chemical characterization of lithium-transition metal borohydride of ($LiZn_2(BH_4)_5$), where they found that ^{11}B MAS NMR peak shifted towards lower frequency (−42 to −46 ppm) compared to the corresponding resonances from $LiBH_4$ (−41.2 ppm). With respect to the comparable electronegativity of Zn (1.6) and Ti (1.5) [51], ^{11}B MAS NMR peak of lithium–titanium borohydride is approaching to that of lithium–zinc borohydride (−42 to −46 ppm) [50]. Therefore, it can be assumed that ^{11}B MAS NMR signal centered at −46.2 ppm (Fig. 7(b)) is in accordance with lithium–titanium borohydride. The products after nanoconfinement, i.e., eutectic $LiBH_4$–$Mg(BH_4)_2$ and lithium–titanium borohydride, are considered as low dehydrogenation temperature phases as previous reports [47,52,53]. Therefore, the onset dehydrogenation at 140 °C as well as lower polymeric phase transformation temperature (81 and 91 °C) found in DSC thermogram (Fig. 2(B)) of nanoconfined $2LiBH_4$–MgH_2–$0.13TiCl_4$ can be attributed to the eutectic $LiBH_4$–$Mg(BH_4)_2$ and lithium–titanium borohydride formed during nanoconfinement. Regarding the ^{11}B MAS NMR peak area, the main phase performing low temperatures of phase transformation and dehydrogenation is eutectic $LiBH_4$–$Mg(BH_4)_2$ together with some of lithium–titanium borohydride. In the case of the products after desorption, the lineshape, markedly affected by second-order quadrupolar interactions, can be attributed to the signal of boric acid ($B(OH)_3$) or B_2O_3 units [49] (Fig. 7(c)). This refers to the interaction of boron, produced after dehydrogenation, with oxygen in ambient environment. Furthermore, the signals of MgB_2 and $[B_{12}H_{12}]^-$, centered at 95.3 and -15.5 ppm, respectively [47,54] cannot be detected after dehydrogenation (Fig. 7(c)). It can be assumed that most of MgH_2 and $Mg(BH_4)_2$ (from eutectic $LiBH_4$–$Mg(BH_4)_2$) decompose to form Mg. In conclusion, three-step dehydrogenation of nanoconfined $2LiBH_4$–MgH_2–$0.13TiCl_4$ belongs to (i) eutectic $LiBH_4$–$Mg(BH_4)_2$ and lithium–titanium borohydride (at 140 °C), (ii) flexible and reactive $LiBH_4$ solvated by LiCl (at 240 °C) and (iii) MgH_2 (at 380 °C).

For rehydrogenation under 130 bar H_2, LiCl signal is enhanced at about 120 °C (Fig. 8). By heating the dehydrogenated sample to 377 °C, the formations of Ti–MgH_2 alloys ($Mg_{0.25}Ti_{0.75}H_2$ [55] and Mg_6TiH_2 [56]) and unknown phase are observed. It has been reported that desorption kinetics of MgH_2 is improved after alloy formation with transition metals [55,56]. Thus, the formations of $Mg_{0.25}Ti_{0.75}H_2$ and Mg_6TiH_2 after 1st rehydrogenation could develop the dehydrogenation kinetics during the 2nd cycle as compared with nanoconfined $2LiBH_4$–MgH_2, in agreement with titration measurements in Fig. 4. After rehydrogenation, the reflections of $LiBH_4$ are not found by cooling the sample to room temperature (Fig. 8). It can be due to the fact that either $LiBH_4$ is not reversible or it is nanoconfined in $TiCl_4$–CAS. Thus, rehydrogenated sample of nanoconfined $2LiBH_4$–MgH_2–$0.13TiCl_4$ was further investigated by FTIR.

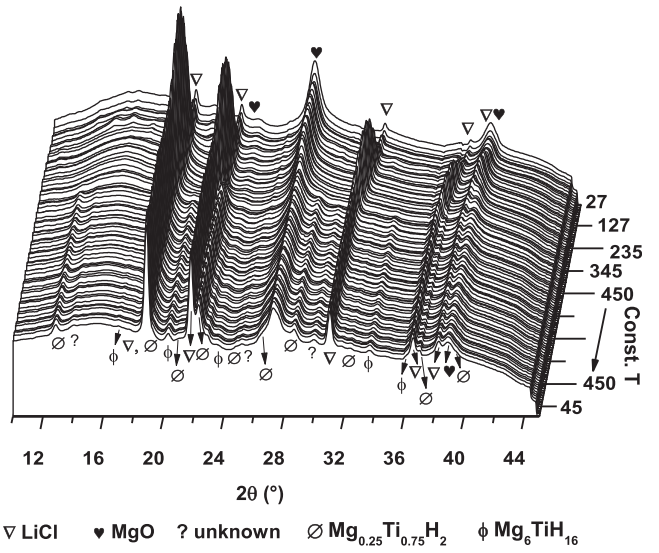

Fig. 8. SR-PXD patterns of nanoconfined $2LiBH_4$–MgH_2–$0.13TiCl_4$ rehydrogenation (T = 450 °C, dT/dt = 10 °C/min, and $p(H_2)$ = 130 bar).

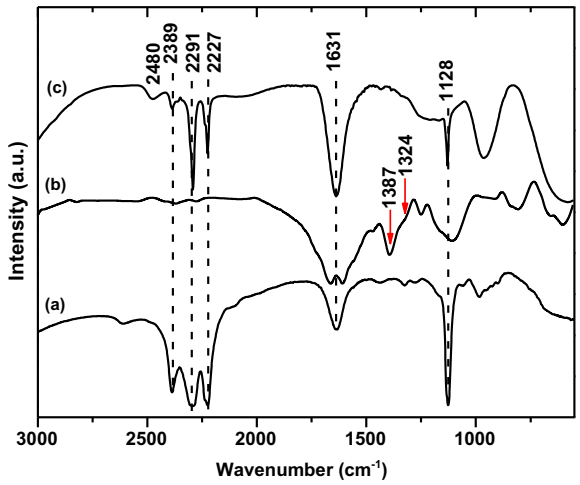

Fig. 9. FT-IR spectrum of pristine $LiBH_4$ (a), nanoconfined $2LiBH_4$–MgH_2–$0.13TiCl_4$ after dehydrogenation (b) and rehydrogenation (c).

In order to investigate other possible phases formed after dehydrogenation as well as to confirm the formation of $LiBH_4$ after rehydrogenation, dehydrogenated and rehydrogenated powder samples of nanoconfined $2LiBH_4$–MgH_2–$0.13TiCl_4$ were further investigated by FTIR. From Fig. 9(a), pristine $LiBH_4$ reveals the characteristic infrared absorption peaks of B–H vibrations at 2389, 2291, 2227 and 1128 cm^{-1}. The peak at 1631 cm^{-1}, in agreement with O–H bond can be attributed to air and moisture contamination during the experiments. Fig. 9(b) exhibits the characteristic peaks of TiH and LiH are observed at 1387 and 1324 cm^{-1}, respectively [57,58]. This hints at the complete dehydrogenation of $LiBH_4$, eutectic $LiBH_4$–$Mg(BH_4)_2$ and lithium–titanium borohydride. For the sample after rehydrogeantion, Fig. 9(c) shows all vibrational

peaks in agreement with pristine $LiBH_4$ (Fig. 9(a)), indicating the reversibility of $LiBH_4$ in nanoconfined $2LiBH_4$–MgH_2–$0.13TiCl_4$ after rehydrogenation. Therefore, the disappearance of $LiBH_4$ phase in SR-PXD patterns of nanoconfined $2LiBH_4$–MgH_2–$0.13TiCl_4$ after rehydrogenation (Fig. 8) could be attributed to the disordered or amorphous phase produced by nanconfinement. Moreover, the vibrational peak of $[B_{12}H_{12}]^{2-}$ at 2480 cm^{-1} [59] is found in the nanoconfined $2LiBH_4$–MgH_2–$0.13TiCl_4$ after rehydrogenation. Since our system includes Mg (from MgH_2) and Li (from $LiBH_4$), the derivatives of $[B_{12}H_{12}]^{2-}$ could be $MgB_{12}H_{12}$ and/or $Li_2B_{12}H_{12}$ [6,60–62]. Thus, the inferior hydrogen content released in the 2nd dehydrogenation to the 1st cycle (Fig. 4) could be explained by the formation of unknown phase and $[B_{12}H_{12}]^{2-}$ derivatives after rehydrogenation.

4. Conclusion

Carbon aerogel scaffold (CAS) prepared from cross-linked resorcinol-formaldehyde aerogel was embedded with $TiCl_4$ via solution impregnation and further melt infiltrated by hydride composite of $2LiBH_4$–MgH_2 under the molar ratio of $LiBH_4$:MgH_2:$TiCl_4$ as 2:1:0.13 to obtain powder sample, denoted as nanoconfined $2LiBH_4$–MgH_2–$0.13TiCl_4$. It was found that $TiCl_4$ and $LiBH_4$ were successfully nanoconfined in CAS, while MgH_2 proceeded partially. In the same temperature (room temperature-500 °C) and time (about 5 h at constant temperature) ranges, nanoconfined $2LiBH_4$–MgH_2–$0.13TiCl_4$ released up to 99% of theoretical H_2 storage capacity, while that of nanoconfined $2LiBH_4$–MgH_2 was only 94%, suggesting considerable kinetic improvement. Moreover, dehydrogenation rate was approximately two times faster after $TiCl_4$ doping, for example, to desorb 3.6 wt.% H_2 during 1st dehydrogenation, nanoconfined $2LiBH_4$–MgH_2–$0.13TiCl_4$ required 1 h 30 min, while that of nanoconfined $2LiBH_4$–MgH_2 needed 3 h 30 min. With respect to in situ SR-PXD and ^{11}B MAS NMR results, the formations of lithium–titanium borohydride and eutectic $LiBH_4$–$Mg(BH_4)_2$ were observed after melt infiltration as well as no decomposition of MgH_2. For gas analysis during dehydrogenation, hydrogen was released in three steps at 140, 240, and 380 °C with no traces of toxic diborane (B_2H_6) gas together with small amount of other gases related to humidity and methylene chloride (solvent of commercial $TiCl_4$ solution). Significant reduction of onset dehydrogenation temperature of nanoconfined $2LiBH_4$–MgH_2–$0.13TiCl_4$ (at 140 °C) as compared with those of nanoconfined $2LiBH_4$–MgH_2 (280 °C, reported in this work) and $2LiBH_4$–MgH_2–$TiCl_3$ (250 °C, reported in reference [33]) as well as low polymeric phase transformation temperature (81 and 91 °C) was attributed to lithium–titanium borohydride and eutectic $LiBH_4$–$Mg(BH_4)_2$. For the second and the third steps of dehydrogenation at 240 and 380 °C, decompositions of destabilized $LiBH_4$ due to LiCl solvation and MgH_2 were detected, respectively. The dehydrogenation products were composed of B, Mg, TiH, and LiH. After the 1st rehydrogenation, the formations of Ti–MgH_2 alloys ($Mg_{0.25}Ti_{0.75}H_2$ and Mg_6TiH_2), well-known active phases for desorption kinetic improvement of MgH_2, were observed, yielding the superior kinetics during the 2nd dehydrogenation of nanoconfined $2LiBH_4$–MgH_2–$0.13TiCl_4$ to nanoconfined $2LiBH_4$–MgH_2. For the deficient hydrogen storage capacities of the 2nd, 3rd, and 4th cycles as compared with the 1st dehydrogenation, it could be explained by the formations of unknown phase and $[B_{12}H_{12}]^{2-}$ derivatives after the 1st rehydrogenation.

Acknowledgements

The authors would like to acknowledge The Thailand Research Fund and Suranaree University of Technology, Thailand (Project No. TRG5680094) for financial support. Moreover, the work was partially supported by the Danish National Research Foundation (DNRF93) Center for Materials Crystallography, the Danish Strategic Research Council via the research project HyFillFast and by the Carlsberg Foundation. The access to beam time at The MAX-II synchrotron (beam line I711), Lund, Sweden is gratefully acknowledged. Also, we would like to thank Dr. Vittorio Berbenni for very useful FTIR and gas analysis results.

References

[1] A. Züttel, S. Rentsch, P. Fischer, P. Wenger, P. Sudan, P. Mauron, Ch. Emmenegger, J. Alloys Comp. 356–357 (2003) 515–520.
[2] M. Dornheim, S. Doppiu, G. Barkhordarian, U. Bösenberg, T. Klassen, O. Gutfleisch, R. Bormann, Scr. Mater. 56 (2007) 841–846.
[3] M. Dornheim, in: M. Hirscher (Ed.), Handbook of Hydrogen Storage, Wiley–VCH, Weinheim, 2010. pp. 187–214.
[4] G. Barkhordarian, T. Klassen, R. Bormann, Wasserstoff Speicherndes Kompositematerial. Patent German Pub. No.: DE102004/061286, 2004.
[5] J.J. Vajo, S.L. Skeith, F. Mertens, J. Phys. Chem. B 109 (2005) 3719–3722.
[6] U. Bösenberg, S. Doppiu, L. Mosegaard, G. Barkhordarian, N. Eigen, A. Borgschulte, T.R. Jensen, Y. Cerenius, O. Gutfleisch, T. Klassen, M. Dornheim, R. Bormann, Acta. Mater. 55 (2007) 3951–3958.
[7] F.E. Pinkerton, M.S. Meyer, G.P. Meisner, M.P. Balogh, J.J. Vajo, J. Phys. Chem. C 111 (2007) 12881–12885.
[8] M.Q. Fan, L.X. Sun, Y. Zhang, F. Xu, J. Zhang, H.L. Chu, Int. J. Hydrogen Energy 33 (2008) 74–80.
[9] J. Mao, Z. Guo, X. Yu, H. Liu, J. Mater. Res. 26 (2011) 1143–1150.
[10] Y. Zhang, Q. Tian, H. Chu, J. Zhang, L. Sun, J. Sun, Z. Wen, J. Phys. Chem. C 113 (2009) (1969) 21964–21969.
[11] U. Bösenberg, J.W. Kim, D. Gosslar, N. Eigen, T.R. Jensen, J.M. Bellosta von Colbe, Y. Zhou, M. Dahms, D.H. Kim, R. Günther, Y.W. Cho, K.H. Oh, T. Klassen, R. Bormann, M. Dornheim, Acta. Mater. 58 (2010) 3381–3389.
[12] H. Kou, X. Xiao, J. Li, S. Li, H. Ge, Q. Wang, L. Chen, Int. J. Hydrogen Energy 37 (2012) 1021–1026.
[13] X. Xiao, J. Shao, L. Chen, H. Kou, X. Fan, S. Deng, L. Zhang, S. Li, H. Ge, Q. Wang, Int. J. Hydrogen Energy 37 (2012) 13147–13154.
[14] S.T. Sabitu, A.J. Goudy, J. Phys. Chem. C 116 (2012) 13545–13550.
[15] P. Wang, L. Ma, Z. Fang, W. Kang, P. Wang, Energy Environ. Sci. 2 (2009) 120–123.
[16] B.H. Liu, B.J. Zhang, Y. Jiang, Int. J. Hydrogen Energy 36 (2011) 5418–5424.
[17] G.L. Xia, H.Y. Leng, N.X. Xu, Z.L. Li, Z. Wu, J.L. Du, X.B. Yu, Int. J. Hydrogen Energy 36 (2011) 7128–7135.
[18] P. Sridechprasat, Y. Suttisawat, P. Rangsunvigit, B. Kitiyanan, S. Kulprathipanja, Int. J. Hydrogen Energy 36 (2011) 1200–1205.
[19] T.K. Nielsen, U. Bösenberg, R. Gosalawit, M. Dornheim, Y. Cerenius, F. Besenbacher, T.R. Jensen, ACS Nano 4 (2010) 3903–3908.
[20] R. Gosalawit-Utke, T.K. Nielsen, I. Saldan, D. Laipple, Y. Cerenius, T.R. Jensen, T. Klassen, M. Dornheim, J. Phys. Chem. C 115 (2011) 10903–10910.
[21] R. Gosalawit-Utke, T.K. Nielsen, K. Pranzas, I. Saldan, C. Pistidda, F. Karimi, D. Laipple, J. Skibsted, T.R. Jensen, T. Klassen, M. Dornheim, J. Phys. Chem. C 116 (2012) 1526–1534.
[22] G. Capurso, F. Agresti, L. Crociani, G. Rossetto, B. Schiavo, A. Maddalena, S. Lo Russo, G. Principi, Int. J. Hydrogen Energy 37 (2012) 10768–10773.
[23] P. Vajeeston, S. Sartori, K.D. Knudsen, B. Hauback, H. Fjellvåg, J. Phys. Chem. C 116 (2012) 21139–21147.
[24] J.J. Liang, W.C.P. Kung, J. Phys. Chem. B 109 (2005) 17837–17841.
[25] X. Liu, D. Peaslee, C.Z. Jost, E.H. Majzoub, J. Phys. Chem. C 114 (2010) 14036–14041.
[26] P. Ngene, P. Adelhelm, A.M. Beale, K.P. de Jong, P.E. de Jong, J. Phys. Chem. C 114 (2010) 6163–6168.
[27] S. Sartori, K.D. Knudsen, Z. Zhao-Karger, E.G. Bardaji, J. Muller, M. Fichtner, B.C. Hauback, J. Phys. Chem. C 114 (2010) 18785–18789.
[28] J. Gao, P. Adelhelm, M.H.W. Verkuijlen, C. Rongeat, M. Herrich, P.J.M. van Bentum, O. Gutfleisch, A.P.M. Kentgens, K.P. de Jong, P.E. de Jong, J. Phys. Chem. C 114 (2010) 4675–4682.
[29] H.S. Lee, Y.S. Lee, J.Y. Suh, M. Kim, J.S. Yu, Y.W. Cho, J. Phys. Chem. C 115 (2011) 20027–200035.
[30] A. Gross, J.J. Vajo, S.L.V. Atta, G.L. Olson, J. Phys. Chem. C 112 (2008) 5651–5657.
[31] V. Bérube, G. Chen, M.S. Dresselhaus, Int. J. Hydrogen Energy 33 (2008) 4122–4131.
[32] R. Gosalawit-Utke, C. Milanese, T.K. Nielsen, F. Karimi, I. Saldan, K. Pranzas, T.R. Jensen, A. Marini, T. Klassen, M. Dornheim, Int. J. Hydrogen Energy 38 (2013) 1932–1942.
[33] R. Gosalawit-Utke, C. Milanese, P. Javadian, J. Jepsen, D. Laipple, F. Karimi, J. Puszkiel, T.R. Jensen, A. Marini, T. Klassen, M. Dornheim, Int. J. Hydrogen Energy 38 (2013) 3275–3282.
[34] H.R. Hoekstra, J.J. Katz, J. Am. Chem. Soc. 71 (1949) 2488–2492.
[35] M. Au, A. Jurgensen, K. Zeigler, J. Phys. Chem. B 110 (2006) 26482–26487.
[36] M. Au, A.R. Jurgensen, W.A. Spencer, D.L. Anton, F.E. Pinkerton, S.-J. Hwang, C. Kim, R.C. Brwman Jr., J. Phys. Chem. C 112 (2008) 18661–18671.

[37] W.C. Li, A.H. Lu, C. Weidenthaler, F. Schüth, Chem. Mater. 16 (2004) 5676–5681.
[38] J.H. de Boer, B.G. Linsen, Th. Van der Plas, G.J. Zondervan, J. Catal. 4 (1969) 649–653.
[39] G. Halsey, J. Chem. Phys. 16 (1948) 931–932.
[40] S. Brunauer, P. Emmet, E. Teller, J. Am. Chem. Soc. 60 (1939) 309–319.
[41] E.P. Barrett, L.G. Joyner, P.P. Halenda, J. Am. Chem. Soc. 73 (1951) 373–380.
[42] Y. Cerenius, K. Ståhl, L.A. Svesson, T. Ursby, Å. Oskarsson, J. Albertsson, A. Liljas, J. Synchrotron Rad. 7 (2000) 203–208.
[43] B.S. Clausen, G. Steffensen, B. Fabius, J. Villadsen, R. Feidenhans'l, H. Topsøe, J. Catal. 132 (1991) 524–535.
[44] J.A. Rodriguez, J.C. Hanson, A.I. Frenkel, J.Y. Kim, M. Pérez, J. Am. Chem. Soc. 124 (2002) 346–354.
[45] J. Li, X. Wang, Q. Huang, S. Gamboa, P.J. Sebastian, J. Power Sources 158 (2006) 784–788.
[46] L. Mosegaard, B. Møller, J.E. Jørgensen, Y. Filinchuk, Y. Cerenius, J.C. Hanson, E. Dimasi, F. Besenbacher, T.R. Jensen, J. Phys. Chem. C 112 (2008) 1299–1303.
[47] Z. Zhao-Karger, R. Witter, E.G. Bardají, D. Wang, D. Cossement, M. Fichtner, J. Mater. Chem. A 1 (2013) 3379–3786.
[48] K.J.D. MacKenzie, M.E. Smith, "Multinuclear Solid State NMR of Inorganic Materials", Pergamon (2002).
[49] Y. Yan, A. Remhof, P. Mauron, D. Rentsch, Z. Lodziana, Y.-S. Lee, H.-S. Lee, Y.W. Cho, A. Züttel, J. Phys. Chem. C 117 (2013) 8878–8886.
[50] D. Ravnsbæk, Y. Filinchuk, Y. Cerenius, H.J. Jakobsen, F. Basenbacher, J. Skibsted, T.R. Jensen, Angew. Chem. Int. Ed. 48 (2009) 6659–6663.
[51] <http://www.sciencegeek.net/tables/Electronegativity.pdf>.
[52] F. Fang, Y. Li, Y. Song, D. Sun, Q. Zhang, L. Ouyang, M. Zhu, J. Phys. Chem. C 115 (2011) 13528–13533.
[53] B.J. Zhang, B.H. Liu, Z.P. Li, J. Alloys Comp. 509 (2011) 751–757.
[54] C. Pistidda, S. Garroni, F. Dolci, E.G. Bardají, A. Khandelwal, P. Nolis, M. Dornheim, R. Gosalawit, T.R. Jensen, Y. Cerenius, S. Suriñach, M.D. Baró, W. Lohstroh, M. Fichtner, J. Alloys Comp. 508 (2010) 212–215.
[55] S. Er, M.J. van Setten, G.A. de Wijs, G. Brocks, J. Phys. Condens. Matter 22 (2010) 074208.
[56] M.G. Shelyapina, D. Fruchart, P. Wolfers, Int. J. Hydrogen Energy 35 (2010) 2025–2032.
[57] X. Wang, L. Andrews, J. Phys. Chem. A 111 (2007) 6008–6019.
[58] G.V. Chertihin, L. Andrews, J. Am. Chem. Soc. 116 (1994) 8322–8327.
[59] Z. Huang, J. Gallucci, X. Chen, T. Yisgedu, H.K. Lingam, S.G. Shore, J.C. Zhao, J. Mater. Chem. 20 (2010) 2743–2745.
[60] N. Ohba, K. Miwa, M. Aoki, T. Noritake, S. Towata, Y. Nakamori, S. Orimo, A. Züttel, Phys. Rev. B 74 (2006) 075110.
[61] U. Bösenberg, D.B. Ravnsbæk, H. Hagemann, V. D'Anna, C. Bonatto Minella, C. Pistidda, W. von Beek, T.R. Jensen, R. Bormann, M. Dornheim, J. Phys. Chem. C 114 (2010) 15212–15217.
[62] A.D. Kulkarni, L.L. Wang, D.D. Johnson, D.S. Sholl, J.K. Johnson, J. Phys. Chem. C 114 (2010) 14601–14605.